Atomistic theory of electronic and optical properties of InAs/InP self-assembled quantum dots on patterned substrates

Weidong Sheng and Pawel Hawrylak
Institute for Microstructural Sciences, National Research Council of Canada, Ottawa, ON K1A 0R6, Canada

We report on a atomistic theory of electronic structure and optical properties of a single InAs quantum dot grown on InP patterned substrate. The spatial positioning of individual dots using InP nano-templates results in a quantum dot embedded in InP pyramid. The strain distribution of a quantum dot in InP pyramid is calculated using the continuum elasticity theory. The electron and valence hole single-particle states are calculated using atomistic effective-bond-orbital model with second nearest-neighbor interactions, coupled to strain via Bir-Pikus Hamiltonian. The optical properties are determined by solving many-exciton Hamiltonian for interacting electron and hole complexes using the configuration-interaction method. The effect of positioning of quantum dots using nanotemplate on their optical spectra is determined by a comparison with dots on unpatterned substrates, and with experimental results. The possibility of tuning the quantum dot properties with varying the nano-template is explored.
PACS numbers: 73.21.La, 78.67.Hc, 71.15.-m

I. INTRODUCTION

There is currently significant interest in semiconductor self-assembled quantum dots (SAQDs) [1, 2, 3] due to their excellent electronic and optical properties. The quality of optical properties is primarily due to the very clean self-organized Stransky-Krastanow growth process during molecular beam epitaxy. The downside of this process is the random spatial distribution of quantum dots. In order to combine single quantum dots with cavities, gates, or magnetic ions for their increased functionality one needs to position quantum dots by growth on patterned substrates [4].

The patterned substrate growth is both a challenge and opportunity. It is a challenge to assure that patterning of the substrate does not destroy the high quality of single quantum dots, and it is an opportunity to use patterning to control their electronic properties. Recently Williams et al [5, 6] reported high quality emission spectra close to 1.55 μm of single InAs quantum dots grown on InP pyramidal nanotemplate. This opens up the possibility of integration of single quantum dots into optical cavities [7], and hence reliable fabrication of single photon sources [8, 9] suitable for long distance transmission in optical fiber. The theoretical understanding of the effect of patterning on optical spectra is unknown, and we present here atomistic theory of electronic and optical properties of single InAs quantum dot grown on pyramidal InP nanotemplates.

Atomistic calculation of the electronic properties of InAs dots on InP presents a challenge: due to small lattice mismatch between InAs and InP (3%), the InAs dots are significantly larger then InAs dots on GaAs. The larger dot size would suggest the applicability of the $k \cdot p$ method, unfortunately it suffers from the unphysical level crossing as pointed out by Holma et al [10]. Hence atomistic method, which gives proper bulk band dispersion, is needed for InAs/InP dots. In this work, the electron and valence hole single particle states are calculated using atomistic effective-bond-orbital model (EBOM) [11, 12] with second nearest-neighbor interactions, coupled to separately calculated strain distribution via Bir-Pikus Hamiltonian [13]. The optical properties of InAs dots embedded in InP pyramids are calculated by solving the many-exciton Hamiltonian for interacting electron and hole complexes using the configuration-interaction method. The effect of positioning of quantum dots using nanotemplate on their optical spectra is determined by a comparison with dots on unpatterned

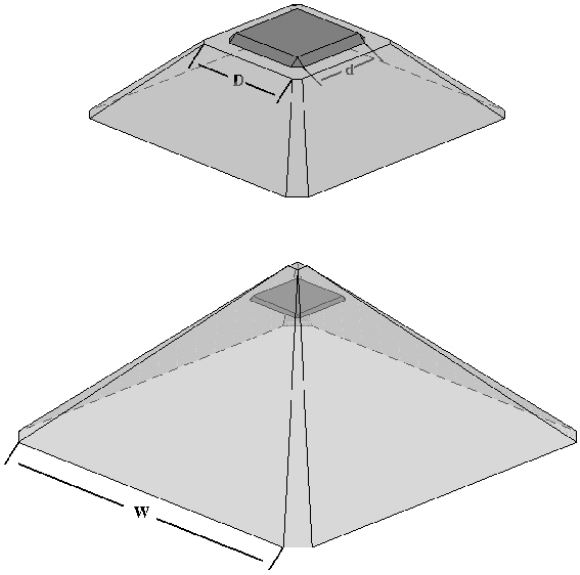

FIG. 1: Single InAs quantum dot on a pyramidal InP nanotemplate (a) before overgrowth, enlarged view of top portion of the structure and (b) after overgrowth.

Electronic address: weidong.sheng@nrc-cnrc.gc.ca

substrates, and with experimental results. The possibility of tuning the optical properties with the shape of the nanotemplate is demonstrated.

II. MODEL OF INAS QUANTUM DOT ON NANOTEMPLATE

In the work of Williams et al [5, 6] the positioning of InAs dots is achieved by first the growth of InP nanotemplate with controlled size and shape, followed by the growth of a single InAs dot, as shown in Fig. 1. The quantum dot is covered by continuing the growth of InP, with the final result of a single InAs dot embedded in an InP pyramid. There is experimental evidence [5] that the shape and size of the template determines the geometry of the dot. Hence for a rectangular template, including facets associated with [100] and [111] crystallographic axis shown in Fig. 1, we model the dot as a rectangular InAs box, with truncations around its four corners.

In this calculation, we chose the size of the template as $D = 46$ nm, the lateral size of the dot as $d = 36$ nm, with height of $h = 2.35$ nm [14]. After overgrowth, the dot ends up embedded 18 nm below the top of the pyramid, as shown in the lower panel of Fig. 1. The size and the shape of the nanotemplate (denoted by W in Fig. 1) can be varied. The pyramid fabricated in Refs. [5, 6] had $W = 400$ nm. In this exploratory example, we chose a smaller size of the pyramidal template, $W = 206$ nm with height $h = 103$ nm to reduce significant computational effort.

III. ATOMISTIC TIGHT-BINDING APPROACH TO ELECTRONIC STRUCTURE

Electronic structure of InAs/InP dots has been calculated in the past using the quasicontinuous eight-band $k \cdot p$ method [15]. For atomistic calculations, the empirical tight-binding method (ETBM) [16] is a natural choice. However, considering that InAs/InP dots are generally much larger than InAs/GaAs dots due to smaller lattice mismatch, we chose EBOM due to its less requirement of computational resources and a compatibility with the $k \cdot p$ method. EBOM is a sp^3 tight-binding method in which the full symmetry of zinc-blende lattice is reduced to that of a fcc lattice. The one electron tight-binding Hamiltonian describes an electron hopping from atomic orbital α at position R to orbital α' at position R':

$$H_{tb} = \sum_{R,\alpha;R',\alpha'} H(R,\alpha;R',\alpha') c^{+}_{R,\alpha} c_{R',\alpha'}; \qquad (1)$$

where $c^{+}_{R,\alpha}$ ($c_{R',\alpha'}$) are creation (annihilation) operators. The hopping matrix elements and site energies for s and p orbitals, extended to include second nearest-neighbor interactions, are given in real space by

$$\begin{aligned}
H(R,s;R',s) &= E_{ss}^{000}\,\delta_{R,R'} + E_{ss}^{110}\,\delta_{R-R',\tau} + E_{ss}^{200}\,\delta_{R-R',\eta};\\
H(R,p;R',p) &= \delta_{R-R',\tau}\left[E_{xx}^{110}\,\tau_p^2 + E_{xx}^{011}(1-\tau_p^2)\right]\\
&\quad + \delta_{R-R',\eta}\left[E_{xx}^{200}\,\tau_p^2 + E_{xx}^{002}(1-\tau_p^2)\right]\\
&\quad + E_{xx}^{000}\,\delta_{R,R'};\\
H(R,p;R',p') &= E_{xy}^{110}\,\tau_p\,\tau_{p'}\,\delta_{R-R',\tau};\\
H(R,s;R',p) &= E_{sx}^{110}\,\tau_p\,\delta_{R-R',\tau}; \qquad (2)
\end{aligned}$$

where τ and η give positions of the nearest and second-nearest neighbors, respectively,

$$\begin{aligned}
\tau &= \frac{a}{2}(-1,-1,0),(-1,0,-1),(0,-1,-1);\\
\eta &= a(-1,0,0),(0,-1,0),(0,0,-1); \qquad (3)
\end{aligned}$$

a is the lattice constant.

There are ten fitting parameters, E_{ss}^{000}, E_{ss}^{110}, E_{ss}^{200}, E_{sx}^{110}, E_{xx}^{000}, E_{xx}^{110}, E_{xx}^{011}, E_{xx}^{200}, E_{xx}^{002}, E_{xy}^{110} in EBOM. The two-center approximation [17] introduces an additional constraint, $E_{xx}^{110} - E_{xy}^{110} = E_{xx}^{011}$. With second nearest-neighbor interactions included [18], effective masses of electrons and holes at the Γ point [10, 19], conduction and valence band edges at both the Γ and X points [20] can be exactly fitted within EBOM. With increasing k, it can reproduce correct band dispersion along the Γ–X direction [21], as shown in Fig. 2.

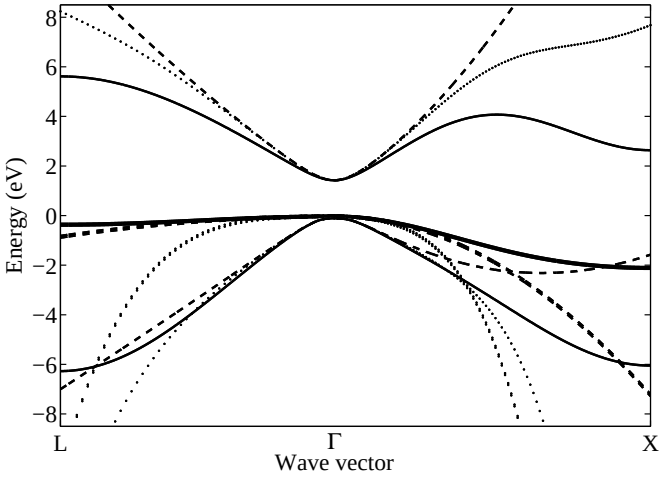

FIG. 2: Band structure of InP described by the eight-band $k \cdot p$ method (dotted lines) and its modified version (dash lines, see text), compared with that by the tight-binding-like EBOM (solid lines).

Compared with the eight-band $k \cdot p$ method, one of advantages of the EBOM is the absence of spurious crossing between valence bands (see Fig. 2). To alleviate this deficiency in the $k \cdot p$ method, terms proportional to $(k_x^4 + k_y^4 + k_z^4)$ are proposed [10] to be added to heavy-hole and light-hole bands to eliminate the resulting spurious solutions (see dash line in Fig. 2). Although this modification does not alter effective masses at the

point, it is nevertheless seen to give unphysical dispersion of valence bands along the X and L directions, compared with that given by the EBOM.

When EBOM is applied to two different materials, a band offset between the unstrained island and matrix material is needed to obtain all the fitting parameters. The effect of strain is incorporated into EBOM through the deformation potential Bir-Pikus's theory [12, 13] and through the piezoelectric effect. An advantage of the EBOM over ETBM is its lack of ambiguity in fitting the deformation potential parameters [22].

IV. STRAIN DISTRIBUTION

The strain in the vicinity of quantum dot is determined by the position of the quantum dot in the pyramid. Hence the domain of strain calculation should include the entire pyramid, with characteristic sizes on the micron scale. While the full atomistic and finite element calculation for the quantum dot and the pyramid will be implemented in the future, we report here calculations based on continuum elasticity theory [23]. We enclose the template in a rectangular computational box. A fixed boundary condition is applied to the base of the template while free-standing boundary conditions are implemented to all the other exposed facets. This is achieved by introducing dummy sites around the template where infinitesimal elastic constants are assigned, therefore, the force applied to the template facets can be neglected. The quality of results of continuum elasticity theory calculations are successfully verified by comparison with the results of atomistic valence-force-field calculations [24] for smaller structures.

The strain tensor is obtained by minimizing the following elastic energy functional

$$E = \frac{1}{2}\int C_{11}\left(\varepsilon_{xx}^2+\varepsilon_{yy}^2+\varepsilon_{zz}^2\right)+C_{44}\left(\varepsilon_{xy}^2+\varepsilon_{yz}^2+\varepsilon_{zx}^2\right) + 2C_{12}\left(\varepsilon_{xx}\varepsilon_{yy}+\varepsilon_{yy}\varepsilon_{zz}+\varepsilon_{zz}\varepsilon_{xx}\right) d^3r; \quad (4)$$

where C_{11}, C_{44}, and C_{12} are elastic constants of quantum dot material and of InP pyramid material, the values of which are taken from Ref. [10].

Figure 3 shows two typical strain components, hydrostatic and biaxial strain, through the central axis of the dot ([001] direction) and through the center of the dot along the base ([100] direction). The hydrostatic and biaxial strain are defined [19] by

$$H = \varepsilon_{xx}+\varepsilon_{yy}+\varepsilon_{zz};$$

$$B^2 = (\varepsilon_{xx}-\varepsilon_{yy})^2+(\varepsilon_{yy}-\varepsilon_{zz})^2+(\varepsilon_{zz}-\varepsilon_{xx})^2 : (5)$$

The former mainly affects the conduction bands while the latter only affects the valence bands, inducing the splitting between the heavy-hole and light-hole band.

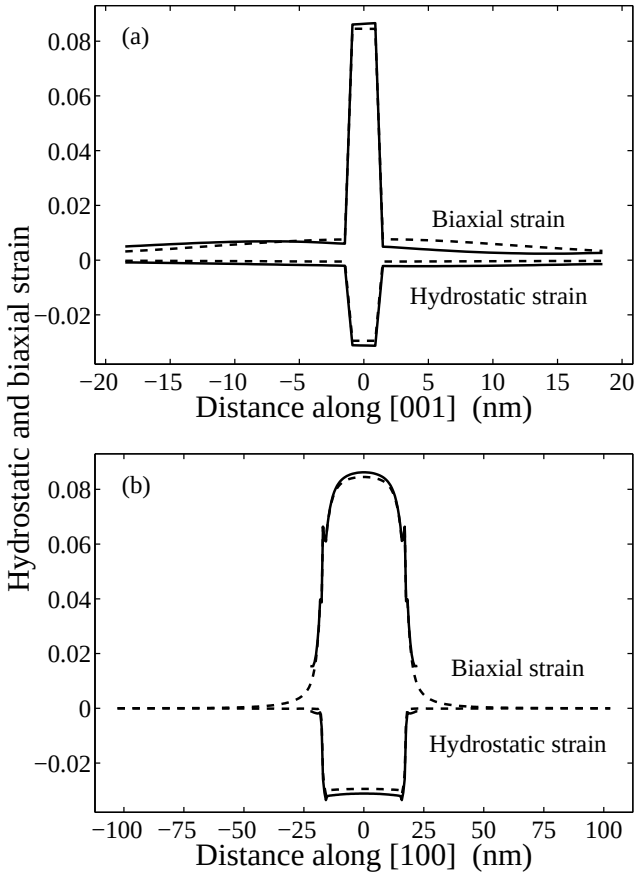

FIG. 3: Plot of hydrostatic and biaxial strain in the InAs/InP quantum dot along the [001] direction towards the apex (a) and along [100] direction (b). For comparison, strain profiles are shown in dash lines for a InAs dot of the same geometry in an unpatterned InP substrate.

The same strain profiles are also shown for InAs dot in an unpatterned InP substrate. In this comparison we assumed the same shape and size of the quantum dot, excluding the possibility that the unpatterned dots are disk-like or lens-shaped. Hereafter, dot on unpatterned substrate is referred to as dot 1 and the dot on patterned substrate is referred to as dot 2.

The comparison between them shows the effect of patterned substrate on the strain distribution. Along the growth direction [see Fig. 3(a)], both the hydrostatic and biaxial strain are found marginally larger in dot 2 than in dot 1, which would lead to a small blue shift of emission energy. Along the direction towards the apex, due to the physical limitation of the patterned substrate, obvious discrepancy can be found between the strain profiles in the two dots that are in different environment. Much less difference is found along the opposite direction where the patterned substrate becomes similar to bulk InP. Along the [100] direction, the strain profiles are found similar for the two dots except for their slightly different peak values.

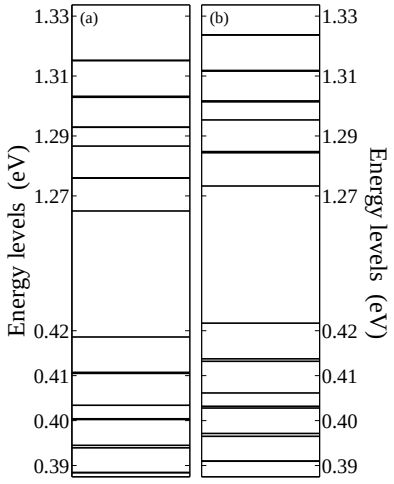

FIG. 4: Energy levels of the single InAs dot on unpatterned InP substrate (a) and on patterned substrate (b) calculated by the EBOM. It is noted that the energy scale in conduction band is different from that in valence bands.

According to the deformation potential theory [13], the local band edges are proportional to the hydrostatic and biaxial strain. If we choose the valence band offset between unstrained InAs and InP as 400 meV [15], the depth of confinement along the growth direction is 420 meV and 530 meV for electrons and holes, respectively, which is in agreement with previous calculation [10]. The heavy-hole band is the top-most valence band, separated from the light-hole band by 150 meV due to the biaxial strain. Although the band offset between unstrained InAs and InP is not well known, it has been shown that the actual electronic structure are not sensitive to the value chosen in the calculation [22].

V. ELECTRONIC STRUCTURE

The computational box for electronic calculation is chosen to be much smaller than that for the strain calculation as we are interested only in the states confined in the dot. It contains the whole dot and some sites outside the patterned substrate where much larger site energies are assigned. Its dimensions are 47.5 nm 47.5 nm 14.1 nm. In EBOM, each unit cell consists of four effective atoms, and each atom has eight spin-orbitals. In total, it gives rise to a large sparse matrix of dimension exceeding five million. The electron states are obtained by solving the sparse matrix using the Lanczos algorithm [19].

Figure 4 (a) and (b) shows the calculated energy levels of electrons and holes by EBOM for dot 1 and 2, respectively. The calculated energy shells are characteristic to the square geometry of the dot, with a single s-level, almost degenerate p-shell, and a d-shell consiting of three states: a single level followed by two degenerate levels.

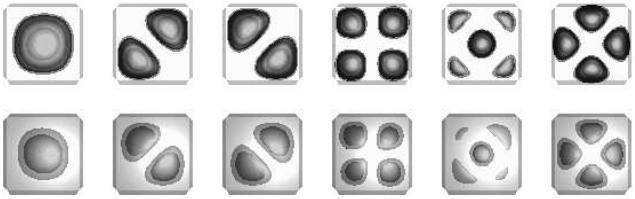

FIG. 5: Probability density of confined electron (upper row) and hole (lower row) states in the dot.

The order and degeneracies (1,2) of levels in the d-shell differentiates the square dot from a lens-shaped (3) or disk-like quantum dot (2,1) studied previously [3], and could be used to infer the shape from the optical spectra.

As can be seen, strain profile specific to nanotemplate (see Fig. 3) induces shifts of energy levels for the dot on patterned substrate. The shift in the conduction band, which is about 11 meV, is more homogeneous than that in the valence bands (about 3 meV) as the latter is also under the influence of other strain components.

The probability density of confined states is shown in Fig. 5. The hole states are found generally more confined than their electron counterparts. Also note that the electron and hole states of p-shell are oriented in the opposite directions. This is a result of piezoelectric potential which attracts electrons while simultaneously repelling holes.

We can label the p-like states according to the extension direction of their wave functions. In the conduction band, the two p-like states are p_+^e and p^e, localized along [110] and [1$\bar{1}$0] directions, with energies $E_{p_+^e} < E_{p^e}$. In the valence bands, the two p-like states, p^h and p_+^h, have a different order, i.e. $E_{p_+^h} < E_{p^h}$ [25].

This inverted order of energy of states with similar symmetry is due to the enhanced piezoelectric effect in the dot on patterned substrate. The piezoelectric potential is calculated from the piezoelectric charge density as given by [19]

$$_P(r) = \quad 2e_{14}\left[\frac{@_{yz}(r)}{@x} + \frac{@_{xz}(r)}{@y} + \frac{@_{xy}(r)}{@z}\right]; \qquad (6)$$

where e_{14} is the piezoelectric constant. Unlike InAs/GaAs dots where e_{14} in GaAs is four times larger than that in InAs, e_{14} in InP is smaller than in InAs.

The left two plots in Figure 6 show the distribution of piezoelectric charge density for the two dots in different environment. The piezoelectric charge in dot 1 is seen to have a nearly symmetric distribution, i.e., a part of positive charge appears in pair with another one of negative charge. The two parts are almost symmetric and hence compensate their effect on electron and hole states, which can be seen in the corresponding piezoelectric potential shown in the upper-right panel. The potential is found to be well localized around the four corners of the dot.

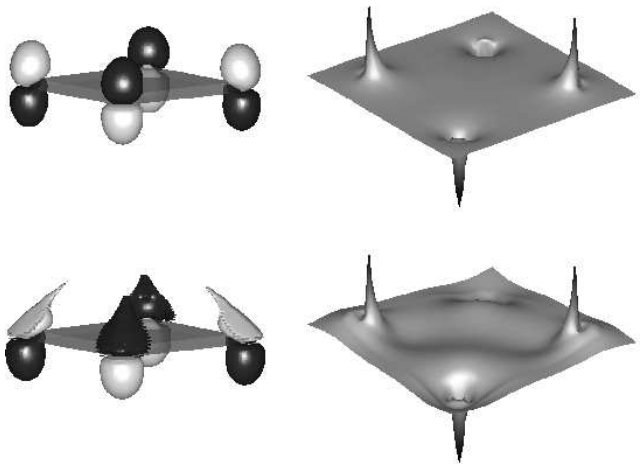

FIG. 6: Effect of nanotemplate: isosurface plots of piezoelectric charge density in the dot on patterned substrate (lower-left plot) and the one on unpatterned substrate (upper-left plot). Bright (dark) grey area has positive (negative) charge. The right plots show the corresponding piezoelectric potentials as seen by an electron along the quantum-dot layer which is about 0.6 nm above the bottom of dots. The peak values of both potentials are about 8 meV.

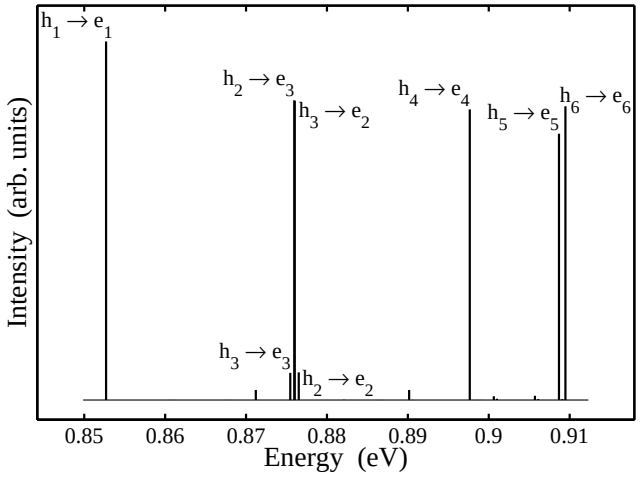

FIG. 7: Intensity of interband transitions between hole and electron states.

Because the positive charge is paired with the negative charge, the potential is very similar to that of dipoles, and is almost zero inside the dot. This leads to only 0.1 meV splitting between the p^e_+ and p^e states.

In dot 2, the piezoelectric charge density is seen to be localized below the dot as well as along the facets of the substrate. This asymmetric distribution of the charge density induces a very different piezoelectric potential. As seen in the lower-right part of Fig. 6, the potential inside the dot has significant value. This leads to a splitting of about 0.5 meV between p^e_+ and p^e, and inverts the order of states in valence bands.

Figure 7 shows the intensity of interband transitions (joined optical density of states) [19] between the calculated hole and electron states. Here, we only plot the transitions polarized within the plane perpendicular to the growth direction, which corresponds to those from the heavy-hole part of the hole states. After the ground state transition, the next two strong transitions are those between the p-like hole and electron states. The transitions between electron and hole states that have different symmetry, i.e., $p^h \to p^e_+$ and $p^h_+ \to p^e$, are seen to have lower intensity.

A further calculation shows that the tight-binding results can be fairly well approximated by a single-band effective-mass approach [21] using the following effective mass parameters, $m_e = 0.065$, $m_h^{001} = 0.32$, and $m_h^{110} = 0.17$. The comparison of these parameters with those of the bulk materials exhibits the effect of strain on the effective mass renormalization in quantum dots. For example, the electron effective mass is enhanced from 0.024 in bulk InAs to 0.065, which is close to the effective mass in bulk InP (0.077). The anisotropy in the hole effective mass tensor is reversed, the holes become much lighter (comparing with 0.639 in bulk InAs and 0.933 in bulk InP) within the plane perpendicular to the growth direction. This results in comparable energy separations in conduction (14.8 meV) and valence (8.0 meV) bands.

VI. EMISSION SPECTRA OF DOTS ON PATTERNED AND UNPATTERNED SUBSTRATES

We now turn to investigate the effect of nano-template growth on electronic states as could be observed from emission spectra as a function of the population of the quantum dot with electrons and holes. The interaction of electrons and holes significantly changes the emission spectra from those expected from the joint optical density of states. The electrons and hole interaction is described via the following Hamiltonian,

$$H_{ex} = \sum_i E^e_i c^+_i c_i + \sum_i E^h_i h^+_i h_i + \sum_{ijkl} V^{he}_{ijkl} h^+_i c^+_j c_k h_l + \frac{1}{2}\sum_{ijkl} V^{ee}_{ijkl} c^+_i c^+_j c_k c_l + \frac{1}{2}\sum_{ijkl} V^{hh}_{ijkl} h^+_i h^+_j h_k h_l; \quad (7)$$

where E^e_i and E^h_i are the energy levels shown in Fig. 4, and V^{ee}, V^{hh}, and V^{he} are the Coulomb matrix elements which can be calculated using the single-particle states as shown in Fig. 5. In the calculation reported below, the multi-exciton configurations are built from the first twelve electron and twelve hole single-particle states (with quasi-spin). These configurations describe the lowest s, p, and d shells. The Hamiltonian is then expanded

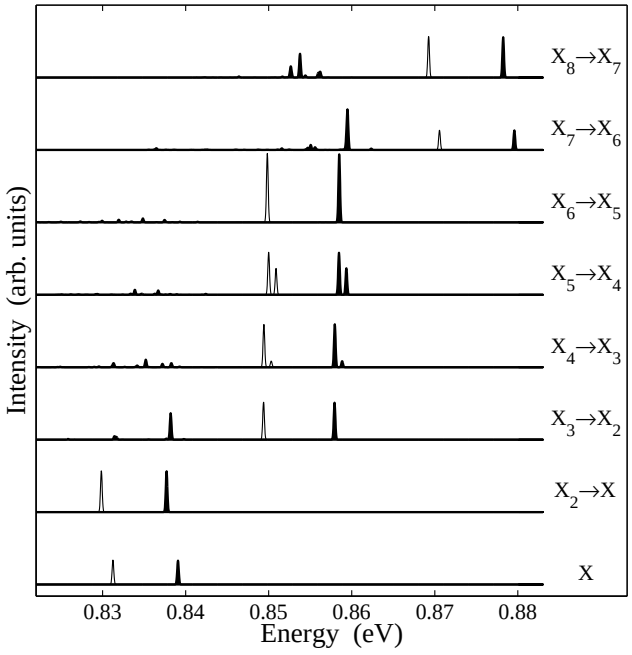

FIG. 8: Emission spectrum from individual multi-exciton complex obtained by solving the many-body Hamiltonian using the configuration-interaction method, shown as peaks filled in dark color. For comparison, the results for the dot on an unpatterned substrate are shown as unfilled peaks.

on these configurations and solved by the configuration-interaction method. For more detailed description of this calculation we refer to our previous work [21].

Figure 8 shows the emission spectra for dot 1 and 2 as a function of photon energy and increasing number of excitons. The emission intensity is calculated for all the possible transitions between the n-exciton complex and (n-1)-exciton complex at a temperature of 4.2 K. The comparison of the spectra between the two dots should show the effect of nano-template, in particular the effect of inverted order of states in the conduction and valence band of the dot on patterned substrate. The inverted order of p-like states in valence bands is due to different strain distribution, especially in the region close to the corners of the dot structure, and hence different piezoelectric potential. However, we find very little difference in the spectra between the two dots except for an overall blue shift which reflects the difference found in the corresponding single-particle energy spectra (see Fig. 4).

Let us first look at tri-exciton which is the first non-trivial case. Fig. 9 illustrates four configurations of the p-shell states for a tri-exciton with definite spin projection in its upper panel. The ground state of the non-interacting tri-exciton complex is given by the configuration $|i\rangle = |p_-^h\, p_+^h\, p_+^e\rangle$ as it has the lowest kinetic energy. The other two configurations $|a\rangle = |p_-^h\, p_+^h\, p_-^e\rangle$ and $|b\rangle = |p_+^h\, p_+^h\, p_+^e\rangle$ have higher kinetic energies due to the splittings between the $p_+^{e(h)}$ and $p_-^{e(h)}$ states. Hence the

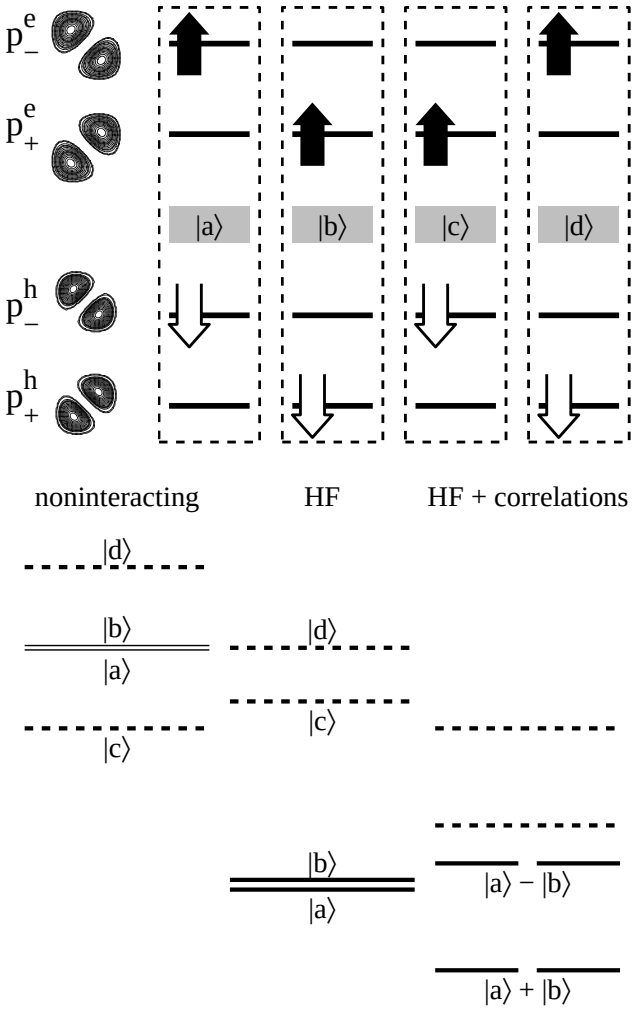

FIG. 9: Upper panel: Four possible configurations of the p-shell states whose probability densities are plotted in the left, Lower panel: Schematic energy levels.

ground state of the non-interacting tri-exciton would be dominated by $|i\rangle$, and is not be optically active. The energies of tri-exciton configurations and a schematic representation of their oscillator strength (solid line – high, dashed line – low) are shown in the lower panel of Fig. 9.

The non-interacting tri-exciton ground state is the dark configuration $|i\rangle$. However, the order of energy levels changes once electron-hole attraction (Hartree-Fock energy) in each configuration is included. As the spatial overlap between p^h and p_+^e is much smaller (see Fig. 4) than either that between p^h and p^e, or that between p_+^h and p_+^e, the corresponding Coulomb interaction is smaller by 2.3 meV compared with those of the other two pairs. Taking this into account, configuration $|i\rangle$ has higher Hartree-Fock energy than $|a\rangle$ and $|b\rangle$ by about 1.8 meV. Configuration $|d\rangle$ has an even higher energy than

$|i\rangle$ because of the splitting between the $p_+^{e(h)}$ and $p^{e(h)}$ states. This arrangement of HF energy levels is shown in lower-central panel of Fig. 9. Once correlation are included (lower-right panel of Fig. 9), the ground state of tri-exciton primarily consists of a symmetric combination of configurations $|a\rangle$ and $|b\rangle$ [26], and becomes optically active.

When the states beyond the second-shell are included, the ground state of four-exciton complex (X_4) is dominated by the singlet-singlet (SS) configuration [26] where the two electrons (holes) occupying the two p-like states have anti-parallel spins. However, a state dominated by a triplet-triplet (TT) configuration is lying very close to the ground state. Hence, there are two emission peaks found in the p-shell emission spectrum of 4X. Depending on the temperature and spin relaxation, the emission from this excited state may become stronger. The ground state of five-exciton complex is well isolated from excited states. The two emission peaks found in the p-shell are the result of recombinations to the ground and first excited 4X states. The emission spectrum from s and p shells for dot on patterned substrate is very similar to the dot on unpatterned substrate. Hence patterning did not deteriorate optical properties.

A. Power-dependent emission

In the experiment [5], the emission spectra are measured as a function of excitation power and include the contribution from all the multi-exciton complexes. In our calculation, we solve the rate equations [27] for given excitation power to obtain the distribution probability of each multi-exciton complex. The overall emission spectra are computed by the summation of the contribution from individual multi-exciton complex weighted by the calculated probabilities.

Figure 10 shows the dependence of photoluminescence spectrum on the excitation power controlled by dimensionless parameter P. The first emission line appearing in the s shell is from the single exciton and the second line is from a bi-exciton. The calculated single exciton emission line is about 15 meV below what the experiment measured. The calculated bi-exciton binding energy (measured by the separation between the X and X_2 lines) is 1.4 meV, which is larger than what the experiment measured (0.9 meV).

In the s shell between the X and X_2 lines lies an emission line from the tri-exciton. As the excitation power increases, the emission from the p shell is seen to have larger intensity than the s shell. In the p shell, the major emission peaks from X_3 (X_5) and X_4 (X_6) overlap each other due to their very similar emission energies (see also Fig. 8). In addition, emission from higher-lying states beyond the p-shell can also be seen at higher energies, which is characteristic to that from a single 2s level of the d-shell, populated by one and two electron-hole pairs, much like an s-shell.

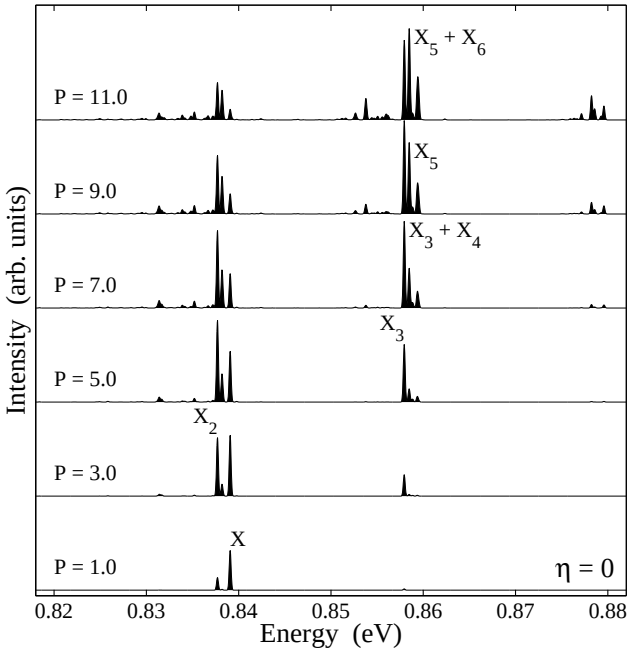

FIG. 10: The calculated photoluminescence spectra at various excitation power P (in arbitrary units). The major individual emission peaks are labeled according to their origin.

The energy separation between the emission lines of the single exciton and tri-exciton defines the separation of the s and p shell. Compared with the experimental value [5], which is about 18.0 meV, our calculation gives 17.9 meV. This shell separation is largely determined by the lateral size of the dot and not sensitive to the height of the dot.

VII. TUNING OPTICAL PROPERTIES WITH NANOTEMPLATE

We now turn to the possibility of tuning the shape of a quantum dot with the shape of the template. We assume that the change in the template leads to the controlled elongation of the quantum dot. The degree of elongation is defined as $= (d - d^0)/d$ where d and d^0 denote the dimensions of the rectangular base of the elongated dot. We keep d as a constant (36 nm) and change d^0 to obtain different elongated geometries.

To explain the effect of elongation on the emission spectrum we discuss here in detail the emission from the five-exciton complex. Even without elongation the emission from the 5X complex results in two emission lines in the p-shell, as shown in Fig. 8. These two lines originate from two different 4X states: singlet-singlet (SS) and triplet-triplet (TT) 4X states [26]. The splitting between the SS and TT states is mainly determined by the competition between exchange energy of triplets and correlations in singlet-singlet configurations. When there is

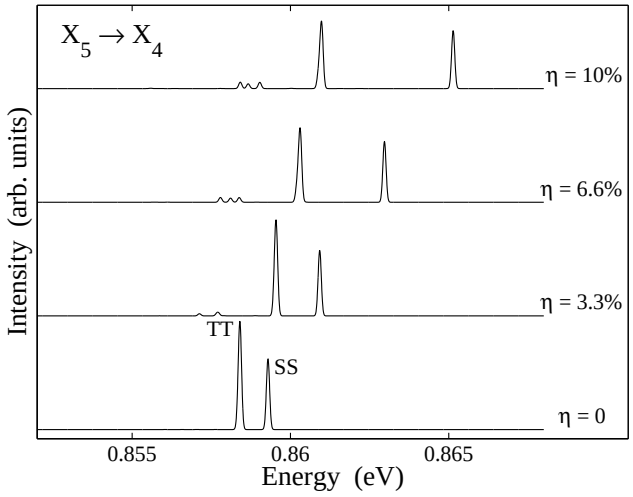

FIG. 11: Emission spectra of the five-exciton complex in quantum dots with increasing elongation

elongation in the geometry of the dot, the almost degenerate single-particle states in the p-shell have an extra splitting proportional to the elongation. This splitting is present in the splitting of the SS and TT states of 4X complex, which can be seen in the emission spectrum of 5X. This is illustrated in Fig. 11 which shows the dependence of emission spectra on the elongation of the structure.

The splitting between the two emission peaks of 5X is seen to increase with the degree of elongation, which can be well explained by the increasing splitting between the single-particle states in the p-shell. The emission peaks of all the multi-exciton complexes are found to have blue shifts as the degree of elongation increases, which is due to the shrinking of the volume of the quantum dot.

We summarize the effect of the elongation on the emission spectra as a function of excitation power in Fig. 12 which shows the emission spectra for an elongated dot with $\eta = 6.6\%$. While the elongation is seen not to affect the emission in the s-shell, the splittings it induced in the p-shell can be clearly identified. The order of individual emission peaks in the p-shell is also found sensitive to the elongation.

VIII. CONCLUSIONS

In conclusion, we have presented a theoretical study of electronic and optical properties of a single InAs dot on InP patterned substrate. We have calculated the strain distribution in nanotemplate with appropriate boundary conditions. By applying the atomistic tight-binding effective-bond-orbital method, we have obtained the electronic structure of the dot on patterned substrate. By comparing the results with those for the dot on unpatterned substrate, we have shown that the patterned substrate breaks the reflection symmetry of the structure, enhances the piezoelectric effect, and leads to the inverted order of the p-shell states. We have shown that Coulomb interactions restore the order of electron hole states and result in emission spectra unaffected by the patterning process. We have identified features in the emission spectra which can be related to the shape of the quantum dots, in particular the characteristic emission pattern of the d-shell. We have explored the possibility of tuning the emission spectra by changing the shape of the quantum dot in a controlled way using the nanotemplate. The theoretical results support the notion that the nanotemplate growth of single self-assembled quantum dots is a promising route for the control of the position of self-assembled dots, and hence enables their increased functionality when combined with cavities, magnetic ions, doping and gates. In turn, it is hoped that better experimental control will allow a systematic comparison of microscopic theories with experiment.

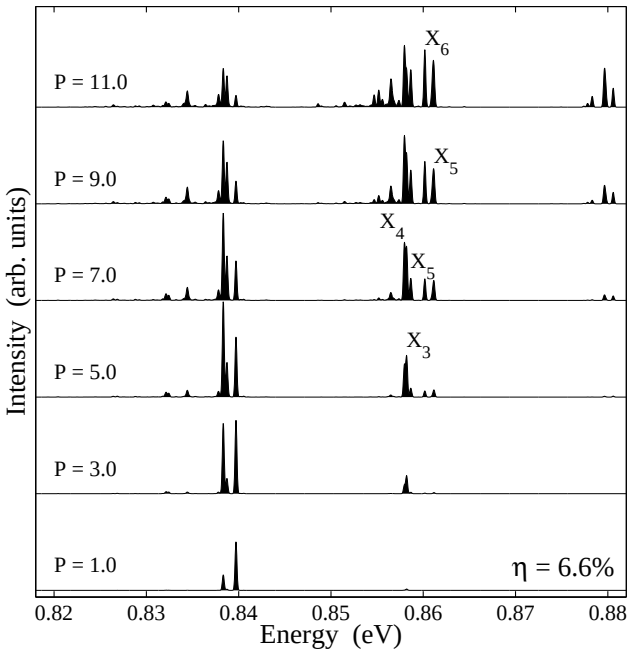

FIG. 12: The photoluminescence spectra at various excitation power P for an elongated dot (= 6:6%).

Acknowledgments

This work is supported by the NRC HPC project, NRC-HELMHOLTZ grant, and Canadian Institute for Advanced Research. The authors would like to thank R. L. Williams and G. C. Aers for discussions.

[1] Lucjan Jacak, Pawel Hawrylak, and Arkadiusz Wojs, Quantum dots, (Springer, Berlin, New York, 1998).
[2] D. Bimberg, M. Grundmann, and N. N. Ledentsov, Quantum Dot Heterostructures, (John Wiley & Sons, UK, 1998).
[3] P. Hawrylak and M. Korkusinski, Electronic properties of self-assembled quantum dots, in Single Quantum dots, edited by P. Michler (Springer, Berlin, New York, 2003).
[4] S. Ishida, Y. Arakawa, and K. Wada, Appl. Phys. Lett. 72, 800 (1998).
[5] R. L. Williams, G. C. Aers, J. Lefebvre, P. J. Poole and D. Chithrani, Physica E 13, 1200 (2002).
[6] D. Chithrani, R. L. Williams, J. Lefebvre, P. J. Poole, and G. C. Aers, Appl. Phys. Lett. 84, 978 (2004).
[7] Dan Dalacu, Daniel Poitras, Jacques Lefebvre, Philip J. Poole, GeofC. Aers, and Robin L. Williams, Appl. Phys. Lett. 84, 3235 (2004).
[8] J. Kim, O. Benson, H. Kan, and Y. Yamamoto, Nature (London) 397, 500 (1999).
[9] O. Benson, C. Santori, M. Pelton, and Y. Yamamoto, Phys. Rev. Lett. 84, 2513 (2000).
[10] M. Holma, M.-E. Pistol, and C. Pryor, J. Appl. Phys. 92, 932 (2002).
[11] Yia-Chung Chang, Phys. Rev. B 37, 8215 (1988).
[12] Sophia J. Sun and Yia-Chung Chang, Phys. Rev. B 62, 13631 (2000).
[13] G. L. Bir and G. E. Pikus, Symmetry and Strain-Induced Effects in Semiconductors, (Wiley, New York, 1974).
[14] J.P. McCaffrey, M. D. Robertson, P. J. Poole, B. J. Riel, and S. Fafard, J. Appl. Phys. 90, 1784 (2001).
[15] H. Pettersson, C. Pryor, L. Landin, M.-E. Pistol, N. Carlsson, W. Seifert, and L. Samuelson, Phys. Rev. B 61, 4795 2000.
[16] S. Lee, L. Jonsson, J.W. Wilkins, G. W. Bryant, and G. Klimeck, Phys. Rev. B 63, 195318 (2001).
[17] John P. Loehr, Phys. Rev. B 50, 5429 (1994)
[18] I. Vurgaftman and J. R. Meyer, Phys. Rev. B 64, 245207 (2001).
[19] H. Jiang and J. Singh, Phys. Rev. B 56, 4696 (1997); Craig Pryor, Phys. Rev. B 57, 7190 (1998); O. Stier, M. Grundmann, and D. Bimberg, Phys. Rev. B 59, 5688 (1999); Weidong Sheng and J.-P. Leburton, Appl. Phys. Lett. 80, 2755 (2002).
[20] G. Klimeck, R. C. Bowen, T. B. Boykin, T. A. Cwik, Superlattices and Microstructures, 27, 519 (2000).
[21] Weidong Sheng, S.-J. Cheng, Pawel Hawrylak, Phys. Rev. B, 71, 035316 (2005).
[22] R. Santoprete, Belita Koiller, R. B. Capaz, P. Kratzer, Q. K. K. Liu, and M. Scheffler, Phys. Rev. B 68, 235311 (2003).
[23] C. Pryor, J. Kim, L. W. Wang, A. J. Williamson, and A. Zunger, J. Appl. Phys. 83, 2548 (1998).
[24] J. Groenen, C. Priester, and R. Carles, Phys. Rev. B 60, 16013 (1999).
[25] The energy of hole states is measured from the top of valence bands in bulk GaAs.
[26] Pawel Hawrylak, Phys. Rev. B 60, 5597 (1999).
[27] E. Dekel, D. Gershoni, E. Ehrenfreund, J.M. Garcia, and P. M. Petroff, Phys. Rev. B 61, 11009 (2000).